



Cite this: *Nanoscale*, 2023, **15**, 3991

## A clinically translatable kit for MRI/NMI dual-modality nanoprobe based on anchoring group-mediated radiolabeling†

Lei Chen,<sup>‡a</sup> Yun Gao,<sup>‡a</sup> Jianxian Ge,<sup>a</sup> Yi Zhou,<sup>a</sup> Zhe Yang,<sup>a</sup> Cang Li,<sup>a</sup> Baoxing Huang,<sup>a</sup> Kuan Lu,<sup>a</sup> Dandan Kou,<sup>a</sup> Dandan Zhou,<sup>a</sup> Can Chen,<sup>a</sup> Sixia Wang,<sup>a</sup> Shuwang Wu,<sup>a</sup> Jianfeng Zeng,<sup>‡\*a</sup> Gang Huang<sup>b</sup> and Mingyuan Gao<sup>\*a,b,c</sup>

Magnetic resonance imaging (MRI)/nuclear medicine imaging (NMI) dual-modality imaging based on radiolabeled nanoparticles has been increasingly exploited for accurate diagnosis of tumor and cardiovascular diseases by virtue of high spatial resolution and high sensitivity. However, significant challenges exist in pursuing truly clinical applications, including massive preparation and rapid radiolabeling of nanoparticles. Herein, we report a clinically translatable kit for the convenient construction of MRI/NMI nanoprobe relying on the flow-synthesis and anchoring group-mediated radiolabeling (LAGMERAL) of iron oxide nanoparticles. First, homogeneous iron oxide nanoparticles with excellent performance were successfully obtained on a large scale by flow synthesis, followed by the surface anchoring of diphosphate-polyethylene glycol (DP-PEG) to simultaneously render the underlying nanoparticles biocompatible and competent in robust labeling of radioactive metal ions. Moreover, to enable convenient and safe usage in clinics, the DP-PEG modified nanoparticle solution was freeze-dried and sterilized to make a radiolabeling kit followed by careful evaluations of its *in vitro* and *in vivo* performance and applicability. The results showed that <sup>99m</sup>Tc labeled nanoprobe are effectively obtained with a labeling yield of over 95% in 30 minutes after simply injecting Na[<sup>99m</sup>TcO<sub>4</sub>] solution into the kit. In addition, the Fe<sub>3</sub>O<sub>4</sub> nanoparticles sealed in the kit can well stand long-term storage even for 300 days without deteriorating the colloidal stability and radiolabeling yield. Upon intravenous injection of the as-prepared radiolabeled nanoprobe, high-resolution vascular images of mice were obtained by vascular SPECT imaging and magnetic resonance angiography, demonstrating the promising clinical translational value of our radiolabeling kit.

Received 27th October 2022,

Accepted 16th January 2023

DOI: 10.1039/d2nr05988f

rsc.li/nanoscale

## Introduction

Cancer and cardiovascular diseases have been severely threatening the lives of human beings and nowadays have become the major cause of human death. To precisely diagnose these diseases, particularly at their earlier stages, comprehensive information about both anatomic and functional abnormality

of the disease sites is essentially required. To this end, different imaging modalities have been combined to extract more information per scan.<sup>1</sup> Among the paramount imaging modalities, magnetic resonance imaging (MRI) exhibits the advantages of providing anatomic information with high spatial resolution with unlimited detection depth of the body,<sup>2</sup> while nuclear medicine imaging (NMI), including positron emission tomography (PET) and single-photon emission computed tomography (SPECT), is apt to give quantitative information apart from its high specificity and sensitivity.<sup>3–5</sup> Therefore, a PET/MRI hybrid scanner has been invented, as an example for unifying the advantages of both MRI and NMI, to harness the strengths of PET and MRI to produce highly detailed pictures of the body.<sup>6–8</sup> Nevertheless, such MRI/NMI dual-modality imaging device hasn't been used to its maximum worthiness due to the lack of well-matching imaging probes.<sup>9</sup> To the best of our knowledge, there are no clinical MRI/NMI dual-modality probes so far, thereby leaving

<sup>a</sup>Center for Molecular Imaging and Nuclear Medicine, State Key Laboratory of Radiation Medicine and Protection, School for Radiological and Interdisciplinary Sciences (RAD-X), Soochow University, Collaborative Innovation Center of Radiological Medicine of Jiangsu Higher Education Institutions, Suzhou 215123, China. E-mail: jfzeng@suda.edu.cn, gaomy@suda.edu.cn

<sup>b</sup>Shanghai Key Laboratory of Molecular Imaging, Shanghai University of Medicine and Health Sciences, Shanghai 201318, China

<sup>c</sup>The Second Affiliated Hospital of Soochow University, Suzhou 215004, China

† Electronic supplementary information (ESI) available. See DOI: <https://doi.org/10.1039/d2nr05988f>

‡ These authors contributed equally to this work.

great room for developing advanced MRI/NMI dual-modality probes.<sup>10</sup>

Due to the tunable physicochemical properties that allow for the flexible introduction of radionuclides and other types of functional moieties, ultra-small superparamagnetic iron oxide (USPIO) nanoparticles with well-proven MRI applications are demonstrated to be the ideal platform and have been successfully used for constructing MRI/NMI dual-modality molecular imaging probes.<sup>11–14</sup> Nevertheless, to promote the clinical translation of USPIO-based MRI/NMI nanoprobe, it is very essential to develop a radiolabeling kit that can alleviate the issues encountered in research such as lengthy procedure, radiation exposure, and risk of human error while still following a good radiopharmacy practice.<sup>15,16</sup> However, the realization of such USPIO-based radiolabeling kits remains challenging.

A facile and reliable radiolabeling method is primarily needed to prepare the USPIO-based radiolabeling kits. To date, numerous radiolabeling methods have been developed accordingly, which can be generally divided into two categories, *i.e.*, incorporating radionuclides into the crystalline lattice of the USPIO nanocrystal core (intrinsic radiolabeling)<sup>17–20</sup> and coupling the radionuclides on the particle surface *via* the secondary chelating moieties or specific moieties of surface capping ligands (extrinsic radiolabeling).<sup>21–25</sup> For example, <sup>59</sup>Fe,<sup>26</sup> <sup>89</sup>Zr,<sup>27</sup> <sup>111</sup>In<sup>28</sup> and <sup>64</sup>Cu<sup>29</sup> have been directly doped into the lattice of USPIO nanoparticles with a high radiolabeling stability. However, long radiolabeling time and high reaction temperatures are usually required to accomplish radiolabeling or improve the radiolabeling yield, which are unfeasible in the case of introducing short half-life radionuclides and bioactive molecules. In addition, as strict radiation protections are essentially required throughout the whole synthesis and purification processes, it becomes experimentally more complicated to achieve the radiolabeling of USPIO through intrinsic radiolabeling. In comparison, extrinsic radiolabeling can achieve quick labeling under mild conditions such as <sup>64</sup>Cu,<sup>21</sup> <sup>177</sup>Lu<sup>23</sup> and <sup>68</sup>Ga<sup>24</sup> through the secondary chelating groups of the ligands anchored on the particle surface. However, to effectively avoid the radionuclide from falling off from nanoparticles, which may cause inaccurate diagnostic outcomes, remains challenging.<sup>26,30</sup> In short, all aforementioned methods fail to simultaneously satisfy the requirements of clinical translation in terms of simplicity, efficiency, and stability. To address these issues, we have previously reported a ligand anchoring group mediated radiolabeling (LAGMERAL) method for rapid and effective labeling of inorganic nanoparticles with metallic radioisotopes, mediated by the strong chelating ability of a diphosphate anchoring groups of the particle surface ligands.<sup>31</sup> This LAGMERAL method is not only facile and efficient, but also suitable for labeling different kinds of inorganic nanoparticles with various types of radionuclides.<sup>32</sup> Therefore, further developing a radiolabeling kit based on LAGMERAL shows very bright prospects for the clinical translation of this innovative method.

Apart from the labeling method itself, another important prerequisite for developing a radiolabeling kit for creating MRI/NMI dual-modality imaging nanoprobe is the massive and reproducible production of USPIO nanoparticles.<sup>33</sup> So far, the high-temperature thermal decomposition approach has been widely accepted as a reliable method for producing high-quality USPIO nanoparticles and large scale production of high-quality USPIO nanoparticles through single batch synthesis has already been achieved. For example, Park *et al.* developed a versatile method for synthesizing uniform-sized nanoparticles *via* the thermal decomposition of iron oleate complexes, and as much as 40 g of nanoparticles could be obtained in one batch.<sup>34</sup> However, as the particle size and morphology are very sensitive to experimental conditions and synthetic parameters,<sup>12,35,36</sup> reproducibility is still one of the biggest obstacles that hinder the clinical translation of USPIO-based nanodrugs. Flow synthesis, which allows the continuous preparation of products, is an alternative solution for the massive production of USPIO nanoparticles. To date, various functional nanomaterials such as Fe<sub>3</sub>O<sub>4</sub> nanoparticles,<sup>37</sup> NaGdF<sub>4</sub>:Yb,Er nanoparticles,<sup>38</sup> perovskite quantum dots,<sup>39</sup> and Au nanorods<sup>40</sup> have been successfully prepared through the flow synthesis. Owing to the advantages of minimized variations of synthetic parameters and no man-made intervention, flow synthesis can hopefully overcome the reproducibility issues of USPIO nanoparticles with the aid of an automated continuous synthetic system,<sup>37,41</sup> providing scalable and sufficient materials for repeatable preparation of a radiolabeling kit from a final translatable perspective.

Herein, we report a clinically translatable kit for constructing MRI/NMI dual-modality nanoprobe depending on the LAGMERAL method. USPIO nanoparticles with uniform size, excellent performance, and large-scale production capacity were first synthesized *via* high-temperature thermal decomposition using a flow synthesis system, and then modified by diphosphate-polyethylene glycol (DP-PEG) *via* ligand exchange to impart good water-solubility and radiolabeling capacity. The resulting nanoparticles-containing aqueous solution is freeze-dried into solid powder and sealed into an ampoule under the protection of nitrogen to allow convenient sterilization, storage, transportation, and radiolabeling. And then the well-designed radiolabeling kit was carefully investigated by DLS and other tests on its stability and reliability for clinical usage with a pretty long shelf time. Moreover, the clear display of micro-vessels in vascular SPECT imaging and magnetic resonance angiography demonstrates the potential clinical translational value of our radiolabeling kit.

## Materials and methods

### Chemicals

All chemicals and reagents were used as received without any further purification. Ferric acetylacetonate (Fe(acac)<sub>3</sub>), oleic acid, and oleyl amine were purchased from Aladdin Biochemical Technology Co., Ltd. Isopropanol, tetrahydro-

furan (THF), acetone, and cyclohexane were purchased from Sinopharm Chemical Reagent Co., Ltd. Tin(II) chloride dihydrate was purchased from Alfa Aesar (China) Chemical Co., Ltd. Diphosphonate PEG (DP-PEG) was provided by Suzhou Xinying Bio-Medical Technology Co., Ltd.  $\text{Na}^{99\text{m}}\text{TcO}_4$  was purchased from Shanghai GMS Pharmaceutical Co., Ltd. Milli-Q water with a resistivity above 18 M $\Omega$  cm was used in the experiments.

### Characterization

Transmission electron microscopy (TEM) images were recorded on FEI Tecnai G2 microscopes working at an accelerating voltage of 120 kV. The hydrodynamic size was measured at 25 °C with a Malvern Zetasizer Nano ZS90 equipped with a solid-state He–Ne laser ( $\lambda = 633$  nm). The X-ray diffraction (XRD) pattern was recorded using a Bruker D8 advance diffractometer under Cu K $\alpha$ 1 radiation ( $\lambda = 1.54056$  Å). The iron concentration was determined by the 1,10-phenanthroline spectrophotometric method after the resulting nanoparticles were digested by HCl. In all experiments, the concentration of  $\text{Fe}_3\text{O}_4$  nanoparticles was defined by the Fe content.

### Synthesis of hydrophobic $\text{Fe}_3\text{O}_4$ nanoparticles

The hydrophobic  $\text{Fe}_3\text{O}_4$  nanoparticles were prepared by flow synthesis. Typically, 8.33 g (23.6 mmol) of  $\text{Fe}(\text{acac})_3$ , 40.1 g (142 mmol) of oleic acid, and 38.0 g (142 mmol) of oleylamine were dissolved in 1 L of isopropanol. The resulting stock solution was purged with nitrogen for 10 min, and then pumped into a stainless steel tube reactor at a reaction temperature of 269 °C, a pressure of 5.1 MPa, and a flow rate of 200 mL  $\text{min}^{-1}$ . The residence time was 3 minutes. After cooling down, the reaction solution was directly centrifuged to obtain crude  $\text{Fe}_3\text{O}_4$  nanoparticles. After re-dispersion in cyclohexane followed by precipitation with ethanol for three cycles, the nanoparticles were kept in cyclohexane for further experiments.

### Ligand exchange

Typically, 60 mg of DP-PEG was dissolved in 3 mL of THF containing 10 mg (*ca.*) hydrophobic  $\text{Fe}_3\text{O}_4$  nanoparticles. Then, the reaction mixture was heated to 40 °C and maintained at this temperature for 48 h under stirring. After that, the  $\text{Fe}_3\text{O}_4$  nanoparticles were precipitated by cyclohexane, washed with cyclohexane three times, and then dried under vacuum at room temperature. Then, the PEGylated  $\text{Fe}_3\text{O}_4$  nanoparticles, denoted as  $\text{Fe}_3\text{O}_4@$ DP-PEG, were dissolved in water. To remove excess PEG ligands, the resulting aqueous solution was subjected to ultrafiltration for 3 cycles using a 100 kDa MWCO centrifugal filter (Millipore YM-100).

### Preparation of radiolabeling kits

In the ampoule, 10  $\mu\text{L}$   $\text{SnCl}_2$  solution (1 mg  $\text{mL}^{-1}$ , dissolved in 0.1 M HCl) was added and lyophilized. Then, 200  $\mu\text{g}$  of freeze-dried  $\text{Fe}_3\text{O}_4@$ DP-PEG nanoparticle powder was added to the ampoule that contained  $\text{SnCl}_2$ . The ampoule was purged with  $\text{N}_2$  gas for 2 minutes before sealing, and then irradiated at a dose of 25 kGy for sterilization.

### Relaxivity measurements

The relaxivity measurements were carried out on a 3 T pre-clinical MRI scanner. A series of concentrations of  $\text{Fe}_3\text{O}_4$  nanoparticles aqueous solutions in 2 mL Eppendorf tubes were prepared. The MPRAGE sequence was used to measure  $T_1$ . The measurement parameters were set as follows: TR = 10 000 ms, TE = 5 ms, and TI = 500–3500 ms (with 500 ms intervals). MEMS sequence was used to measure  $T_2$ , and its parameters were TR = 1400 ms and TE = 15–150 ms (with 15 ms intervals).

### Preparation of $\text{Fe}_3\text{O}_4@^{99\text{m}}\text{Tc}$ -DP-PEG nanoprobe

Briefly, 200  $\mu\text{L}$   $\text{Na}^{99\text{m}}\text{TcO}_4$  solution with a radioactivity of 74 MBq (2 mCi) was injected into the radiolabeling kit to dissolve the nanoparticle powder under slight shaking. Then the mixture was reacted at room temperature for 5–30 min to complete the radiolabeling.

### Radiolabeling yield

To determine the radiolabeling yield, the  $\text{Fe}_3\text{O}_4@^{99\text{m}}\text{Tc}$ -DP-PEG nanoprobe obtained by the kit were further purified by ultrafiltration using a 30 kDa MWCO centrifugal filter. The radiolabeling yield of  $\text{Fe}_3\text{O}_4$  nanoparticles was calculated according to the following equation

$$\text{Radiolabeling yield} = \frac{R_{\text{USPIO}}}{R_{\text{radionuclide}}} \times 100\%$$

where  $R_{\text{radionuclide}}$  and  $R_{\text{USPIO}}$  are the radioactivities of radionuclide added and purified  $\text{Fe}_3\text{O}_4@^{99\text{m}}\text{Tc}$ -DP-PEG nanoprobe, respectively.

### Radiolabeling stability assessment

To evaluate the radiolabeling stability, the purified  $\text{Fe}_3\text{O}_4@^{99\text{m}}\text{Tc}$ -DP-PEG nanoprobe were incubated in water, PBS, or FBS. Aliquots were extracted at different time points for monitoring the radiochemical purities, which can be evaluated by ultrafiltration. Typically, 10  $\mu\text{L}$  of the sample was mixed with 2 mL of Milli-Q water and then ultrafiltered to below 100  $\mu\text{L}$  using a 30 kDa MWCO centrifugal filter. The radioactivity of the residue remaining in the filter and the filtrate were measured with a gamma counter. The radiochemical purity was determined by comparing the activity retained in the filter with the total activity.

### Experimental animal

Specific pathogen free (SPF) grade BALB/c female mice were purchased from Changzhou Cavens Laboratory Animal Co., Ltd. All animal procedures were performed in accordance with the guidelines for the Care and Use of Laboratory Animals of Soochow University and approved by the Animal Ethics Committee of Soochow University.

### SPECT-CT imaging and pharmacokinetics

SPECT/CT imaging was performed using an animal SPECT with an integrated CT system (MILabs, Utrecht, the Netherlands). BALB/c mice (5–6 weeks old, ~20 g) were

anesthetized with 5% isoflurane and then intravenously injected with a freshly prepared solution of radioactive probes. SPECT-CT images were acquired with a U-SPECT+/CT from MILabs equipped with an extra ultra-high sensitivity collimator (54 pinholes, reconstructed resolution 1.0 mm, sensitivity >12 500 cps per MBq) at different time points post-injection. Anesthesia was maintained with 1.5% isoflurane (300 mL min<sup>-1</sup>) during the imaging experiments. The SPECT-CT images were reconstructed using the software package provided by MILabs and then analyzed using PMOD software. Quantification was performed by selecting the volume of interest (VOI) of the desired organs/tissues using the quantification tool of the PMOD software.

### *In vivo* MR imaging

The MR images were acquired on a 3 T pre-clinical MRI scanner. BALB/c mice were anesthetized and injected *via* the tail vein with the Fe<sub>3</sub>O<sub>4</sub>@DP-PEG nanoparticles (5.6 mg per kg body weight). Then, the 3D FLASH sequence was performed for the magnetic resonance angiography. The following parameters were used: TR = 10 ms, TE = 0; FA = 30°, coronal slice orientation, field of view = 35 × 35 mm<sup>2</sup>, matrix = 128 × 128, slice thickness/gap = 0.25/0 mm and NEX = 1. ImageJ software was used to reconstruct the obtained images according to the maximum intensity projection (MIP) protocol.

## Results and discussion

To realize the clinical translation of USPIO-based MRI/NMI dual-modality nanoprobe, the primary prerequisite is to stably obtain USPIO in large quantities. However, so far, most of the high-quality USPIO nanoparticles were synthesized in batch reactors with poor reproducibility and low production efficiency, largely hindering industrialization.<sup>37</sup> To make the synthesis easily scalable and minimize the batch-to-batch variation, herein a continuous synthetic strategy was adopted on the basis of our previous investigations on flow synthesis of inorganic nanoparticles.<sup>42</sup> Fig. 1a shows the schematic of a flow synthesis system in the current study. By using this setup, the hydrophobic USPIO nanoparticles can be continuously obtained by thermal decomposition of ferric acetylacetonate (Fe(acac)<sub>3</sub>) in the presence of oleic acid and oleylamine in isopropanol. Fig. S1† shows the transmission electron microscopy (TEM) image of the as-prepared nanoparticles. The average particle size is 3.5 nm. The powder X-ray diffraction (XRD) pattern shown in Fig. S2† suggests that the as-prepared USPIO nanoparticles are magnetite. To endow the as-prepared nanoparticles with great water solubility and biocompatibility, the DP-PEG ligand bearing a diphosphonate group at one end and a methoxyl group at the other was taken to replace the hydrophobic ligand on the particle surface to achieve DP-PEG coated Fe<sub>3</sub>O<sub>4</sub> nanoparticles (denoted as Fe<sub>3</sub>O<sub>4</sub>@DP-PEG). The TEM images of Fe<sub>3</sub>O<sub>4</sub>@DP-PEG nanoparticles are presented in Fig. 1b. Careful statistical study (Fig. S3†) suggests that ligand exchange does not alter the size or the size distribution profile

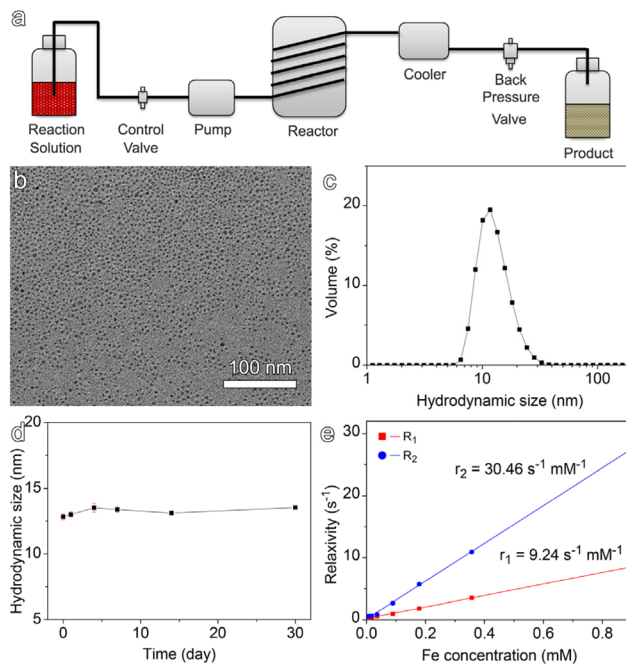


**Fig. 1** Sketch of the flow synthesis of hydrophobic Fe<sub>3</sub>O<sub>4</sub> nanoparticles (a), a representative TEM image of Fe<sub>3</sub>O<sub>4</sub>@DP-PEG nanoparticles (b), together with the hydrodynamic size profiles (c) and colloidal stability (d) of Fe<sub>3</sub>O<sub>4</sub>@DP-PEG nanoparticles. Plots of  $r_1$  and  $r_2$  versus the concentration of Fe<sub>3</sub>O<sub>4</sub>@DP-PEG nanoparticles overlaid with linear fitting curves for extracting longitudinal and transverse relaxivities (e).

of USPIO nanoparticles. Further dynamic light scattering (DLS) result shown in Fig. 1c reveals that the PEGylated nanoparticles exhibit a single scattering peak located at 13.1 nm, indicating that the Fe<sub>3</sub>O<sub>4</sub>@DP-PEG nanoparticles uniformly disperse in water and form no aggregate. Long-term monitoring over 30 days demonstrates that the Fe<sub>3</sub>O<sub>4</sub>@DP-PEG nanoparticles possess excellent colloidal stability in aqueous solution (Fig. 1d). To evaluate the MRI contrast enhancement effects of the Fe<sub>3</sub>O<sub>4</sub>@DP-PEG nanoparticles, the relaxivities were investigated with a clinically relevant 3 T MRI scanner. By linear regression fitting of the experimental data, the longitudinal relaxivity ( $r_1$ ) and transverse relaxivity ( $r_2$ ) are extracted to be 9.2 mM<sup>-1</sup> s<sup>-1</sup> and 30.5 mM<sup>-1</sup> s<sup>-1</sup>, respectively, as shown in Fig. 1e. The  $r_1$  value is 2-fold better than those of commercially available gadolinium-based contrast agents, for instance, 3.2 mM<sup>-1</sup> s<sup>-1</sup> for Magnevist under the same magnetic field. All these data demonstrate that the Fe<sub>3</sub>O<sub>4</sub>@DP-PEG nanoparticles possess satisfactory water solubility, colloidal stability, and relaxivity performance, making the PEGylated Fe<sub>3</sub>O<sub>4</sub> nanoparticles an ideal candidate for the construction of MRI/NMI dual-modality probes. More importantly, based on the continuous synthetic strategy, the production capacity of USPIO nanoparticles can reach 20.0 g h<sup>-1</sup> (based on the Fe content) under the typical conditions used in the current work. The production can be easily scaled up by prolonging the runtime or duplicating the reaction setup, laying a solid foundation for material preparation for the clinical translation of MRI/NMI dual-modality nanoprobe.

For the radiolabeling of  $\text{Fe}_3\text{O}_4$ @DP-PEG nanoparticles, we have recently developed a method, namely, LAGMERAL, which satisfies all the criteria of clinical translation, including easy operation, mild labeling conditions, high efficiency, and high radiolabeling stability. However, to achieve the clinical translation of MRI/NMI dual-modality nanoprobe, there are much more concerns to be considered apart from the radiolabeling method, for instance, the convenient storage and transportation of  $\text{Fe}_3\text{O}_4$ @DP-PEG nanoparticles and the avoidance of unwanted radiation exposure from the whole process of handling and application of radioactive substances. In this case, a radiolabeling kit capable of realizing fast and safe preparation of radiopharmaceuticals provides a reasonable solution.<sup>15,43,44</sup> Therefore, herein we designed a freeze-dried  $\text{Fe}_3\text{O}_4$  nanoparticle-based radiolabeling kit. As shown in Fig. 2a, 10  $\mu\text{L}$  of  $\text{SnCl}_2$  solution containing 10  $\mu\text{g}$   $\text{SnCl}_2$  in 0.1 M HCl was firstly freeze-dried in an ampoule and then 200  $\mu\text{g}$  of freeze-dried  $\text{Fe}_3\text{O}_4$ @DP-PEG nanoparticle powder (calculated by the iron content) was added. The radiolabeling kit was finally obtained after thoroughly purging the ampoule with nitrogen before sealing to avoid the oxidation of  $\text{SnCl}_2$  and  $\text{Fe}_3\text{O}_4$ @DP-PEG nanoparticles (Fig. S4†).

To assess whether or not the freeze-drying process impairs the physicochemical properties of  $\text{Fe}_3\text{O}_4$ @DP-PEG nanoparticles, the solid powder inside the kit was redispersed in water and then analyzed by DLS. As shown in Fig. 2b, the

hydrodynamic size distribution profile of the redispersed  $\text{Fe}_3\text{O}_4$ @DP-PEG nanoparticles show negligible change compared to that of their initially untreated counterparts (Fig. 2b), indicating that the freeze-drying process did not affect the dispersibility of the  $\text{Fe}_3\text{O}_4$ @DP-PEG nanoparticles. The reasonable explanation could lie in the excellent colloidal stability benefited from the robust anchoring capability of PEG ligands. To further verify the radiolabeling efficiency of the kit,  $^{99\text{m}}\text{Tc}$  ( $t_{1/2} = 6$  h) broadly used for SPECT imaging was chosen for demonstration. By simply injecting 200  $\mu\text{L}$  of  $\text{Na}^{99\text{m}}\text{TcO}_4$  solution (2 mCi) into the kit vial as shown in Fig. S5,† the pellet dissolved rapidly after slightly shaking to yield a clear particle-free solution, resulting in the final radiolabeled nanoprobe of nearly unchanged hydrodynamic size as shown in Fig. 2c. In addition, the PDI (0.18 vs. 0.19) and zeta potential value (6.7 mV vs.  $-1.6$  mV) also showed no significant change before and after  $^{99\text{m}}\text{Tc}$  labeling. Specifically, 5 min of incubation at room temperature gave a labeling yield above 90% and it could be elevated beyond 95% if the incubation time was extended to 30 min, which meets the quality assurance requirements for radiopharmaceuticals (Fig. 2d).<sup>45</sup> The extremely high labeling yield allows for direct *in vivo* use of the resulting dual-modality nanoprobe without further purification, due to which the procedure was greatly simplified to shorten the radiation exposure time. Most importantly, the resulting  $^{99\text{m}}\text{Tc}$ -labeled  $\text{Fe}_3\text{O}_4$  nanoparticles (denoted as  $\text{Fe}_3\text{O}_4$ @ $^{99\text{m}}\text{Tc}$ -DP-PEG) exhibit excellent radiolabeling stability either in water, PBS or fetal bovine serum (FBS). As can be seen in Fig. 2e, only 11% of the labeled  $^{99\text{m}}\text{Tc}$  was detached from  $\text{Fe}_3\text{O}_4$  nanoparticles after 24 h of co-incubation with FBS. All of the above results suggest that the radiolabeling kit based on the LAGMERAL method is uniquely advantageous in constructing MRI/NMI dual-modality nanoprobe with excellent radiolabeling stability due to its convenience and efficiency.

To make sure the safe usage of the radiolabeling kit, sterilization is required to eliminate living organisms that may cause adverse effects. Radiation sterilization is considered the optimal method for hermetic kits which are not compatible with other general sterilization techniques such as steam sterilization. Irradiation of 25 kGy as the most validated dose for medical devices was used in this case. However, energy brought by ionizing radiation could also lead to potentially damaging effects on the irradiated materials.<sup>46</sup> For example, gamma radiation is known to destruct the physicochemical properties of biopolymers, resulting in stiffening, softening, embrittlement, *etc.* In this scene, the hydrodynamic size and radiolabeling capability of the irradiated nanoparticles were further studied to figure out whether they are well resistant to radiation. As demonstrated in Fig. 3a and b, irradiation leads to a negligible change in the hydrodynamic size profile and  $^{99\text{m}}\text{Tc}$  labeling yield of the  $\text{Fe}_3\text{O}_4$ @DP-PEG nanoparticles. What's more, following long-term monitoring up to 300 days of storage at room temperature emphasized the excellent stability and reliability of the final kits which can well tolerate the radiation allowing a long shelf life (Fig. 3c and d).

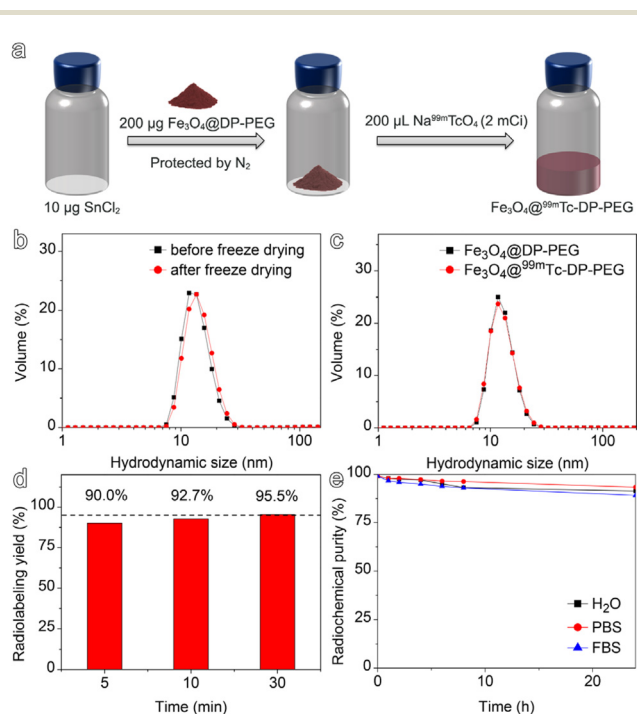


**Fig. 2** Process steps for the fabrication of the  $\text{Fe}_3\text{O}_4$  nanoparticle-based radiolabeling kit (a), hydrodynamic size profiles of the PEGylated particles before and after freeze-drying (b) and  $^{99\text{m}}\text{Tc}$  labeling (c).  $^{99\text{m}}\text{Tc}$  labeling yield of PEGylated particles at different reaction times (d). Radiolabeling stability of the resulting  $\text{Fe}_3\text{O}_4$ @ $^{99\text{m}}\text{Tc}$ -DP-PEG in water, PBS and FBS (e).

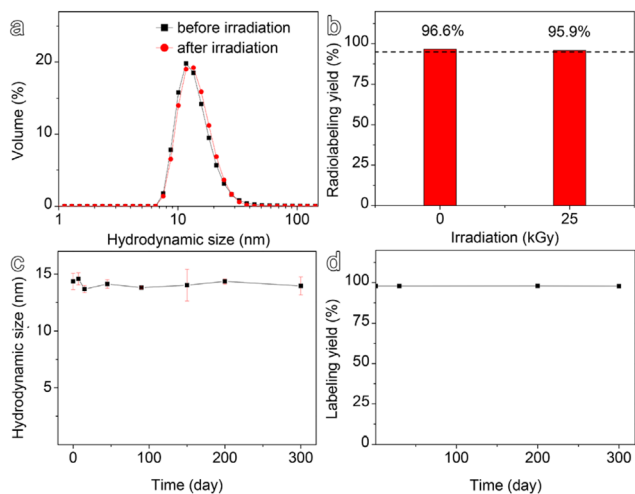


**Fig. 3** Hydrodynamic size profiles (a) and <sup>99m</sup>Tc labeling yield (b) of aqueous solutions of Fe<sub>3</sub>O<sub>4</sub>@DP-PEG nanoparticles before and after irradiation, together with the hydrodynamic size (c) and <sup>99m</sup>Tc labeling yield (d) of Fe<sub>3</sub>O<sub>4</sub>@DP-PEG nanoparticles after irradiation at different storage times.

With the intention of further evaluating the clinical feasibility of the radiolabeling kit, 200 μL of Na<sup>99m</sup>TcO<sub>4</sub> solution (2 mCi) was simply added to dissolve the nanoparticle powder and react for 30 min at room temperature. Then, the obtained Fe<sub>3</sub>O<sub>4</sub>@<sup>99m</sup>Tc-DP-PEG solution was directly intravenously injected into healthy BALB/c mice (corresponding to 5.6 mg Fe per kilogram body weight), which was subsequently subjected to SPECT-CT imaging. The representative images acquired at different time points post-injection are illustrated in Fig. 4a, which demonstrates that the nanoprobe mainly distributes in the blood pool during the initial stage as evidenced by the strong <sup>99m</sup>Tc signal from the heart as well as major blood vessels and vascular organs. With the lapse of time, the <sup>99m</sup>Tc signals start fading from the blood and gradually accumulating in the liver, with a low level of radioactivity remaining in other regions such as the heart, lungs, and kidneys. Furthermore, there is a significant distribution of radioactive signals in the abdominal cavity 1 h post-injection, indicating the accumulation of Fe<sub>3</sub>O<sub>4</sub>@<sup>99m</sup>Tc-DP-PEG nanoprobe in the intestines, which is an obvious characteristic of hepatic metabolism after liver uptake.

For gaining more detailed information about the distribution behavior of the nanoprobe, <sup>99m</sup>Tc signals were quantified by extracting from the volume of interest (VOI) of desired organs or tissues, and expressed as a percentage of the injected dose (%ID) or percentage of the injected dose per cubic centimeters (%ID per cc). As shown in Fig. 4b–g, <sup>99m</sup>Tc presents consistent pharmacokinetic profiles for the heart and lungs, indicating that the radioactivity in the lungs mainly comes from the blood and nearly no uptake of Fe<sub>3</sub>O<sub>4</sub>@<sup>99m</sup>Tc-DP-PEG nanoprobe by the lung occurs. Different from the heart and lungs, the liver and spleen have a continuously high proportion of radioactivity and this situation is quite consistent

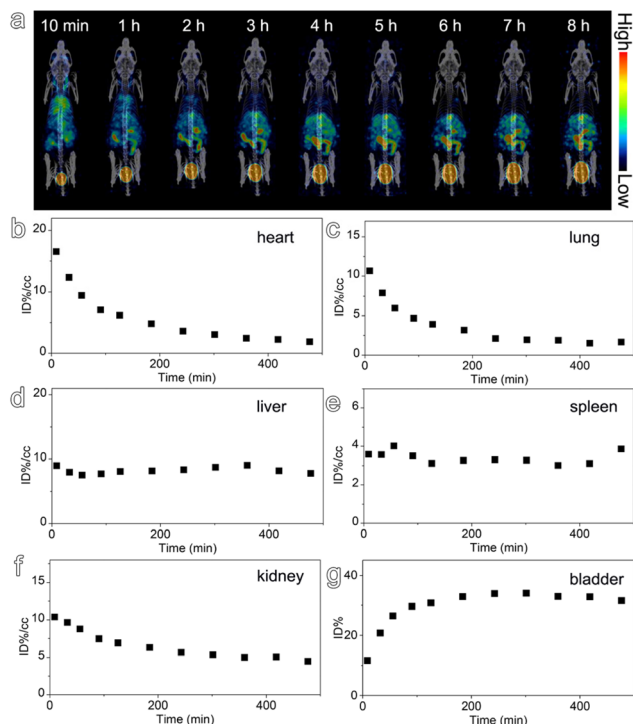


**Fig. 4** SPECT/CT images of mouse intravenously injected with Fe<sub>3</sub>O<sub>4</sub>@<sup>99m</sup>Tc-DP-PEG (a), together with the time-dependent signals of Fe<sub>3</sub>O<sub>4</sub>@<sup>99m</sup>Tc-DP-PEG recorded from different organs such as the heart (b), lungs (c), liver (d), and spleen (e), kidneys (f), and bladder (g).

ent with good knowledge of the reticuloendothelial system capture of nanoparticles. In addition, similar reverse tendencies of <sup>99m</sup>Tc accumulation against time are displayed for the kidneys and bladder. According to the <sup>99m</sup>Tc signal, the particles accumulation in the bladder is more than 30% ID 8 h post-injection, which is much higher than the dissociation rate of <sup>99m</sup>Tc (~6.9%) determined in FBS, suggesting that some of the administered Fe<sub>3</sub>O<sub>4</sub>@<sup>99m</sup>Tc-DP-PEG nanoparticles are excreted *via* the renal clearance pathway. The above pharmacokinetic behaviors for the Fe<sub>3</sub>O<sub>4</sub>@<sup>99m</sup>Tc-DP-PEG nanoprobe obtained using the radiolabeling kit are generally consistent with that of similar nanoprobe in our previous reports where the radiolabeling was performed by using the Fe<sub>3</sub>O<sub>4</sub>@DP-PEG solution,<sup>31,32</sup> demonstrating that the freeze-drying and sterilization processes evolved in the kit preparation also have little impact on the *in vivo* behavior of the resulting radioactive nanoprobe.

By further fitting of the pharmacokinetic profile of the heart, the distribution half-life ( $t_{1/2\alpha}$ ) and elimination half-life ( $t_{1/2\beta}$ ) of the Fe<sub>3</sub>O<sub>4</sub>@<sup>99m</sup>Tc-DP-PEG nanoprobe are determined to be 39.9 min and 256.6 min, respectively. The enough long *in vivo* circulation time which is often a prerequisite for achieving satisfactory targeted accumulation thereof makes the resulting nanoprobe suitable for various diagnostic applications, including tumor imaging, vascular imaging, and so on. In order to verify the practical application effect of the Fe<sub>3</sub>O<sub>4</sub>@<sup>99m</sup>Tc-DP-PEG nanoprobe obtained by the kit, the

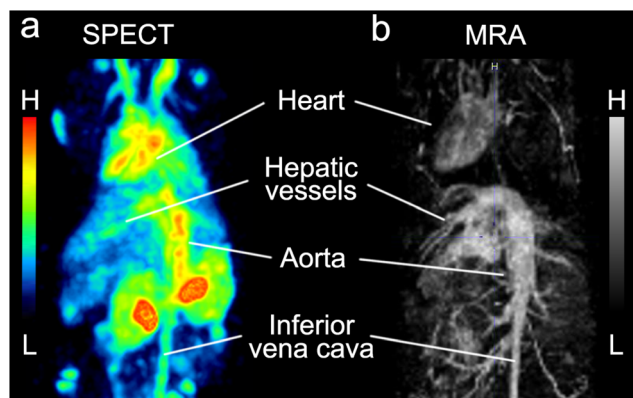


Fig. 5 Vascular SPECT imaging (a) and magnetic resonance angiography (b) of BALB/c mice intravenously injected with  $\text{Fe}_3\text{O}_4@^{99\text{m}}\text{Tc}$ -DP-PEG or  $\text{Fe}_3\text{O}_4@$ DP-PEG at 1 hour, respectively.

MRI/SPECT dual-modality imaging of the vascular system was performed on mice after the probe administration. Fig. 5 shows the representative SPECT and MRI images acquired at 1 h postinjection. As can be seen, with the aid of  $\text{Fe}_3\text{O}_4@^{99\text{m}}\text{Tc}$ -DP-PEG nanoparticles, both SPECT and MRI images allow clear discrimination of the whole-body vessels, such as the hepatic vessels, aorta, and inferior vena cava. In addition, both SPECT and MRI images can be reconstructed to form three-dimensional (3D) animation for better visualization from all angles (available in ESI†). By combining the complementary advantages of SPECT and MRI, it becomes feasible to uncover the subtle changes of the function and structure in the early stage of diseases. Moreover, it is important to extract the diagnostic information from SPECT and MRI at the same time point for reliably monitoring the dynamic process of disease. Thus, the synergy of the two imaging modalities is aimed to provide comprehensive information on the pathological changes to help accurate diagnosis regardless of the asynchronous changes of molecular metabolism and tissue structure, and as well avoid the mismatch of SPECT and MRI images when they are performed in a separated way. Therefore, it can be concluded that the as-prepared radioactive nanoparticles are detectable with both SPECT and MRI imaging techniques, hence are eligible for dual-modality imaging which is expected to achieve an accurate, rapid and sustainable diagnosis of vascular injury and provide a powerful tool for monitoring of pathological processes such as thrombosis therapy, *in vivo* bleeding, and ischemia-reperfusion. In addition, the radiolabeling kit is also expected to have great potential in MRI/NMI dual-modality imaging of tumors as demonstrated in our previous work.<sup>47,48</sup>

## Conclusions

In summary, a clinically translatable radiolabeling kit has been developed for a convenient construction of MRI/NMI

dual-modality nanoprobe based on the anchoring group-mediated radiolabeling method. The  $\text{Fe}_3\text{O}_4$  nanoparticles obtained in a great amount by the continuous synthesis have good stability and high performance, which thus breaks a major barrier to the clinical application. In addition, the  $\text{Fe}_3\text{O}_4$  nanoparticles can retain good colloidal stability and satisfactory radiolabeling yield after either freeze-drying or gamma irradiation, even after a long-term storage of 300 days, laying a solid foundation for the kit development. Due to the robust radiolabeling stability and excellent magnetic properties of the resulting dual-modality nanoprobe, a high-resolution MRI/SPECT vascular image was successfully obtained, showing its outstanding potential in diagnostic imaging applications. In conclusion, we demonstrated that a radiolabeling kit designed based on the LAGMERAL method can be easily and rapidly used to obtain stable MRI/NMI dual-modality probes with excellent clinical translation prospects.

## Author contributions

Chen L. and Gao Y. contributed equally to this work. Conceptualization, Chen L., Gao Y. and Zeng J.; methodology, Chen L., Gao Y., Ge J., Li C. and Huang B.; investigation, Chen L., Gao Y., Ge J., Zhou Y., Yang Z., Li C., Huang B. and Lu K.; writing – original draft preparation, Chen L., Gao Y. and Ge J.; writing – review and editing, Kou D., Zhou D., Chen C., Wang S., Wu S. and Zeng J.; supervision, Wu S., Zeng J., Huang G. and Gao M.; and funding acquisition, Chen L., Zeng J. and Gao M. All authors contributed to the general discussion. The final version of the manuscript was approved by all authors.

## Conflicts of interest

There are no conflicts to declare.

## Acknowledgements

The authors thank the financial support from the National Key Research and Development Program of China (2018YFA0208800), the National Natural Science Foundation of China (82222033, 82130059, 82172003, and 81720108024), the Natural Science Foundation of Jiangsu Higher Education Institutions of China (20KJA150006), the Natural Science Foundation of Jiangsu Province (BK20191418), the Suzhou Key Industry Technology Innovation Projects (SYG202036), the Jiangsu Funding Program for Excellent Postdoctoral Talent (2022ZB589), the special project of “Technological innovation” project of CNNC Medical Industry Co. Ltd (ZHYZD2021006), and the Priority Academic Program Development of Jiangsu Higher Education Institutions (PAPD).

## References

- 1 L. E. Jennings and N. J. Long, *Chem. Commun.*, 2009, 3511–3524.
- 2 R. Qiao, C. Yang and M. Gao, *J. Mater. Chem.*, 2009, **19**, 6274–6293.
- 3 N. K. Devaraj, E. J. Keliher, G. M. Thurber, M. Nahrendorf and R. Weissleder, *Bioconjugate Chem.*, 2009, 397–401.
- 4 L. Li, Y. Wu, Z. Wang, B. Jia, Z. Hu, C. Dong and F. Wang, *J. Nucl. Med.*, 2017, **58**, 821–826.
- 5 B. J. Pichler, A. Kolb, T. Nagele and H. P. Schlemmer, *J. Nucl. Med.*, 2010, **51**, 333–336.
- 6 A. Yilmaz, S. Rosch, H. Yildiz, S. Klumpp and U. Sechtem, *Circulation*, 2012, **126**, 1932–1934.
- 7 O. O. Sogbein, M. Pelletier-Galarneau, T. H. Schindler, L. Wei, R. G. Wells and T. D. Ruddy, *BioMed. Res. Int.*, 2014, **2014**, 942960.
- 8 J. Sanz and Z. A. Fayad, *Nature*, 2008, **451**, 953–957.
- 9 R. Rosales, R. Tavares, A. Glaria, G. Varma, A. Protti and P. J. Blower, *Bioconjugate Chem.*, 2011, **22**, 455–465.
- 10 D. Ni, E. B. Ehlerding and W. Cai, *Angew. Chem., Int. Ed.*, 2019, **58**, 2570–2579.
- 11 L. Sandiford, A. Phinikaridou, A. Protti, L. K. Meszaros, X. J. Cui, Y. Yan, G. Frodsham, P. A. Williamson, N. Gaddum, R. M. Botnar, P. J. Blower, M. A. Green and R. T. M. de Rosales, *ACS Nano*, 2013, **7**, 500–512.
- 12 B. R. Smith and S. S. Gambhir, *Chem. Rev.*, 2017, **117**, 901–986.
- 13 J. Ge, C. Li, N. Wang, R. Zhang, M. J. Afshari, C. Chen, D. Kou, D. Zhou, L. Wen, J. Zeng and M. Gao, *Nanomaterials*, 2022, **12**, 2673–2685.
- 14 L. Jing, C. Yang, P. Zhang, J. Zeng, Z. Li and M. Gao, *View*, 2020, **1**, e19.
- 15 A. Mukherjee, A. Korde, A. Shinto, H. D. Sarma, K. Kamaleswaran and A. Dash, *Appl. Radiat. Isot.*, 2019, **145**, 180–186.
- 16 N. Lepareur, *Front. Med.*, 2022, **9**, 812050.
- 17 R. Weissleder, D. D. Stark, B. L. Engelstad, B. R. Bacon, C. C. Compton, D. L. White, P. Jacobs and J. Lewis, *Am. J. Roentgenol.*, 1989, **152**, 167–173.
- 18 J. Pellico, J. Ruiz-Cabello, M. Saiz-Alia, G. Del Rosario, S. Caja, M. Montoya, L. Fernandez de Manuel, M. P. Morales, L. Gutierrez, B. Galiana, J. A. Enriquez and F. Herranz, *Contrast Media Mol. Imaging*, 2016, **11**, 203–210.
- 19 J. Llop, P. Jiang, M. Marradi, V. Gomez-Vallejo, M. Echeverria, S. Yu, M. Puigivila, Z. Baz, B. Szczupak, C. Perez-Campana, Z. Mao, C. Gao and S. E. Moya, *J. Mater. Chem. B*, 2015, **3**, 6293–6300.
- 20 R. M. Wong, D. A. Gilbert, K. Liu and A. Y. Louie, *ACS Nano*, 2012, **6**, 3461–3467.
- 21 C. Glaus, R. Rossin, M. J. Welch and G. Bao, *Bioconjugate Chem.*, 2010, **21**, 715–722.
- 22 H. Wang, R. Kumar, D. Nagesha, R. I. Duclos Jr., S. Sridhar and S. J. Gately, *Nucl. Med. Biol.*, 2015, **42**, 65–70.
- 23 S. Shanehsazzadeh, C. Grüttner, H. Yousefnia, A. Lahooti, A. Gholami, S. Nosrati, S. Zolghadri, S. H. M. Anijdan, A. Lotfabadi, B. S. Varnamkhasti, F. J. Daha and A. R. Jalilian, *Radiochim. Acta*, 2016, **104**, 2499.
- 24 B. B. Cho, J. H. Park, S. J. Jung, J. Lee, J. H. Lee, M. G. Hur, C. J. Raj and K.-H. Yu, *J. Radioanal. Nucl. Chem.*, 2015, **305**, 169–178.
- 25 Y. Zhao, M. Liang, X. Li, K. Fan, J. Xiao, Y. Li, H. Shi, F. Wang, H. S. Choi, D. Cheng and X. Yan, *ACS Nano*, 2016, **10**, 4184–4191.
- 26 B. Freund, U. I. Tromsdorf, O. T. Bruns, M. Heine, A. Giemsa, A. Bartelt, S. C. Salmen, N. Raabe, J. Heeren, H. Ittrich, R. Reimer, H. Hohenberg, U. Schumacher, H. Weller and P. Nielsen, *ACS Nano*, 2012, **6**, 7318–7325.
- 27 E. Boros, A. M. Bowen, L. Josephson, N. Vasdev and J. P. Holland, *Chem. Sci.*, 2015, **6**, 225–236.
- 28 H. Yuan, M. Q. Wilks, M. D. Normandin, G. El Fakhri, C. Kaittanis and L. Josephson, *Nat. Protoc.*, 2018, **13**, 392–412.
- 29 M. D. Normandin, H. Yuan, M. Q. Wilks, H. H. Chen, J. M. Kinsella, H. Cho, N. J. Guehl, N. Absi-Halabi, S. M. Hosseini, G. El Fakhri, D. E. Sosnovik and L. Josephson, *Angew. Chem., Int. Ed.*, 2015, **54**, 13002–13006.
- 30 W. G. Kreyling, A. M. Abdelmonem, Z. Ali, F. Alves, M. Geiser, N. Haberl, R. Hartmann, S. Hirn, D. J. de Aberasturi, K. Kantner, G. Khadem-Saba, J. M. Montenegro, J. Rejman, T. Rojo, I. R. de Larramendi, R. Ufartes, A. Wenk and W. J. Parak, *Nat. Nanotechnol.*, 2015, **10**, 619–623.
- 31 L. Chen, J. Ge, B. Huang, D. Zhou, G. Huang, J. Zeng and M. Gao, *Small*, 2021, e2104977.
- 32 J. Ge, L. Chen, B. Huang, Y. Gao, D. Zhou, Y. Zhou, C. Chen, L. Wen, Q. Li, J. Zeng, Z. Zhong and M. Gao, *ACS Appl. Mater. Interfaces*, 2022, **14**, 8838–8846.
- 33 P. M. Valencia, O. C. Farokhzad, R. Karnik and R. Langer, *Nat. Nanotechnol.*, 2012, **7**, 623–629.
- 34 J. Park, K. An, Y. Hwang, J. G. Park, H. J. Noh, J. Y. Kim, J. H. Park, N. M. Hwang and T. Hyeon, *Nat. Mater.*, 2004, **3**, 891–895.
- 35 S. Belaid, D. Stanicki, L. Vander Elst, R. N. Muller and S. Laurent, *Nanotechnology*, 2018, **29**, 165603.
- 36 H. J. Kwon, K. Shin, M. Soh, H. Chang, J. Kim, J. Lee, G. Ko, B. H. Kim, D. Kim and T. Hyeon, *Adv. Mater.*, 2018, **30**, e1704290.
- 37 M. Jiao, J. Zeng, L. Jing, C. Liu and M. Gao, *Chem. Mater.*, 2015, **27**, 1299–1305.
- 38 M. Jiao, L. Jing, C. Liu, Y. Hou, J. Huang, X. Wei and M. Gao, *Chem. Commun.*, 2016, **52**, 5872–5875.
- 39 K. Abdel-Latif, F. Bateni, S. Crouse and M. Abolhasani, *Matter*, 2020, **3**, 1053–1086.
- 40 A. Knauer, D. Kuhfuss and J. M. Köhler, *ACS Appl. Nano Mater.*, 2021, **4**, 1411–1419.
- 41 M. Jiao, L. Jing, X. Wei, C. Liu, X. Luo and M. Gao, *Nanoscale*, 2017, **9**, 18609–18612.
- 42 J. Zhang, C. Gong, X. Zeng and J. Xie, *Coord. Chem. Rev.*, 2016, **324**, 39–53.
- 43 M. B. Mallia, A. S. Shinto, M. Kameswaran, K. K. Kamaleswaran, R. Kalarikal, K. K. Aswathy and

- S. Banerjee, *Cancer Biother. Radiopharm.*, 2016, **31**, 139–144.
- 44 M. Asti, M. Iori, P. C. Capponi, S. Rubagotti, A. Fraternali and A. Versari, *Nucl. Med. Commun.*, 2015, **36**, 502–510.
- 45 C. Maioli, G. Luciniani, A. Strinchini, L. Tagliabue and A. Del Sole, *Acta Biomed.*, 2017, **88**, 49–56.
- 46 M. Ahmed, G. Punshon, A. Darbyshire and A. M. Seifalian, *J. Biomed. Mater. Res., Part B*, 2013, **101**, 1182–1190.
- 47 Z. Gao, Y. Hou, J. Zeng, L. Chen, C. Liu, W. Yang and M. Gao, *Adv. Mater.*, 2017, **29**, 1701095.
- 48 J. Zeng, L. Jing, Y. Hou, M. Jiao, R. Qiao, Q. Jia, C. Liu, F. Fang, H. Lei and M. Gao, *Adv. Mater.*, 2014, **26**, 2694–2698.